Organellar relationships in the Golgi region of the pancreatic beta cell line, HIT-T15, visualized by high resolution electron tomography

Brad J. Marsh*, David N. Mastronarde*, Karolyn F. Buttle†, Kathryn E. Howell‡, and J. Richard McIntosh*§

*Boulder Laboratory for 3-D Fine Structure, Department of Molecular, Cellular and Developmental Biology, University of Colorado, Boulder, CO 80309;
†Resource for the Visualization of Biological Complexity, Wadsworth Center, Albany, NY 12201; and ‡Department of Cellular and Structural Biology,
University of Colorado School of Medicine, Denver, CO 80262

This contribution is part of the special series of Inaugural Articles by members of the National Academy of Sciences elected on May 2, 2000

Contributed by J. Richard McIntosh, December 29, 2000

The positional relationships among all of the visible organelles in a densely packed region of cytoplasm from an insulin secreting, cultured mammalian cell have been analyzed in three dimensions (3-D) at ≈6 nm resolution. Part of a fast frozen/freeze-substituted HIT-T15 cell that included a large portion of the Golgi ribbon was reconstructed in 3-D by electron tomography. The reconstructed volume (3.1 × 3.2 × 1.2 μm^3) allowed sites of interaction between organelles, and between microtubules and organellar membranes, to be accurately defined in 3-D and quantitatively analyzed by spatial density analyses. Our data confirm that the Golgi in an interphase mammalian cell is a single, ribbon-like organelle composed of stacks of flattened cisternae punctuated by openings of various sizes [Rambourg, A., Clermont, Y., & Hermo, L. (1979) *Am. J. Anat.* 154, 455–476]. The data also show that the endoplasmic reticulum (ER) is a single continuous compartment that forms close contacts with mitochondria, multiple trans Golgi cisternae, and compartments of the endo-lysosomal system. This ER traverses the Golgi ribbon from one side to the other via cisternal openings. Microtubules form close, non-random associations with the cis Golgi, the ER, and endo-lysosomal compartments. Despite the dense packing of organelles in this Golgi region, ≈66% of the reconstructed volume is calculated to represent cytoplasmic matrix. We relate the intimacy of structural associations between organelles in the Golgi region, as quantified by spatial density analyses, to biochemical mechanisms for membrane trafficking and organellar communication in mammalian cells.

Three-dimensional (3-D) electron microscope (EM) studies have advanced our understanding of the correlation between Golgi organization and the role of this organelle in sorting and trafficking proteins and lipids (1–6). With few exceptions, these studies have used conventional chemical fixation protocols to stabilize cellular components for visualization. Because these methods take anywhere from seconds to minutes to immobilize cellular constituents, labile structures and dynamic events are unlikely to be accurately preserved. Detailed structural study of a rapidly changing organelle like the Golgi should rely on preservation methods like fast freezing that immobilize all cellular activity within milliseconds (7, 8).

We have used high pressure freezing, freeze-substitution, and electron tomography to study the 3-D structure of the Golgi and surrounding organelles in a cell line (HIT-T15) that synthesizes insulin. These cells are often used to study the insulin secretory pathway because they retain the ability to secrete insulin in response to extracellular glucose (9). The relatively low insulin content of these cells (≈300 ng/10^6 cells), compared with normal adult rat pancreas (≈30,000 ng/10^6 cells) (10), permits detailed inspection of the microtubule (MT) cytoskeleton and the organelles involved in membrane traffic, by virtue of the fact that there are fewer granules to obscure other cellular components (11). However, the fact that these cells are modestly granulated has disadvantages. The frequency with which one observes granules attached to, and presumably forming from, the Golgi in samples prepared from HIT-T15 cells under steady state conditions is relatively low. Although we have observed this phenomenon in other reconstructions generated from HIT-T15 cells, it is noteworthy that no granules were attached to the Golgi in the reconstructed volume presented here. This result is despite the fact that the Golgi appears to have been actively budding both clathrin- and non-clathrin-coated vesicles and tubules when the cell was frozen.

In the present study, part of a "representative" insulinoma cell was reconstructed, modeled, and quantitatively analyzed by spatial density analyses. We reasoned that the resulting detailed model would provide a high resolution "3-D snapshot" of the Golgi complex and surrounding organelles in one such cell maintained under steady state conditions. Our results identify some structural features that are similar to those previously observed in normal rat kidney cells (4, 6), whereas other features are novel. The data reveal the 3-D complexity of organellar relationships in the Golgi region of a fast frozen/freeze-substituted regulated secretory cell.

Materials and Methods

Cell Culture. HIT-T15 cells obtained from the American Type Culture Collection (Manassas, VA) were maintained in a humidified incubator (37°C/5% CO_2) in F-12K medium (GIBCO/BRL) supplemented with 10% dialyzed horse serum (GIBCO/BRL), 2.5% FBS (Sigma), L-glutamine (2 mM; GIBCO/BRL), and penicillin (50,000 units)/streptomycin (50 mg; GIBCO/BRL). Medium was replaced every 48 h. Cells were used for experiments before passage 70 to ensure that their ability to synthesize and secrete insulin in response to glucose (24 ng/10^6 cells/24 hr at passage 60) was maintained.

Freezing and Freeze-Substitution. Cells seeded onto Thermanox plastic chips (Nalge Nunc) were cultured for 2–3 days before experiments. Immediately before freezing, each chip was transferred to a brass holding device (Swiss Precision Instruments, Los Angeles) filled with serum-free F-12K medium warmed to 37°C and buffered with Hepes (10 mM). Ficoll (10%; molecular mass 70 kDa) (Sigma) was used as an extracellular cryoprotectant (6). Cells were frozen within ≈10–20 msec under high pressure (≈2,100 atmospheres) by using a Balzers HPM 010 High Pressure Freezer (BAL-TEC, Liechtenstein) and were stored under liquid nitrogen.

Specimens were freeze-substituted with anhydrous acetone (Ernest F. Fullam, Schenectady, NY) containing 0.5% glutar-

---

Abbreviations: 3-D, three-dimensional; EM, electron microscope; ER, endoplasmic reticulum; MT, microtubule.

§To whom reprint requests should be addressed. E-mail: dick@stripe.colorado.edu.

aldehyde/0.1% uranyl acetate (UA) at −90°C for 1–2 days, followed by substitution with acetone containing 1% OsO_4/0.1% UA at −70°C. After specimens were warmed to 0°C over 2–3 days, they were rinsed repeatedly with acetone. Samples were then warmed to room temperature, infiltrated with Embed 812-Araldite resin (Electron Microscopy Sciences, Fort Washington, PA) and flat-embedded. Resin was polymerized at 60°C over 1–2 days.

Microtomy and Microscopy. Cells identified by phase-contrast light microscopy were excised from the resin and remounted in an orientation that permitted *en face* sectioning. Thin (40–60 nm) sections were cut and prepared as previously described (6). Specimens were viewed on a conventional EM operating at 80–100 kV to identify regions of biological interest in well preserved cells for subsequent tomographic study.

Ribbons of serial 400-nm-thick sections were cut and post-stained with 2% aqueous UA and Reynold's lead citrate. Colloidal gold particles (10–15 nm) were deposited on both surfaces of these sections for use as fiducial markers during subsequent image alignment procedures. Selected regions were imaged either at ×15,700 by using a JEM-4000FX intermediate voltage EM (JEOL) operating at 400 kV, or at ×14,690 by using a JEM-1000 high voltage EM operating at 750 kV (JEOL). The grid holding the specimen was tilted at 1.5° intervals over a range of 120° about two orthogonal axes (12). Images at each tilt were collected in series (tilt series) and recorded on film (SO163, Eastman Kodak, or 23D56, Agfa).

3-D Reconstruction. EM negatives were digitized as previously described (6). The positions of fiducial markers on each image were tracked to align the tilt series images with one another by using a modification of the TILTALIGN program that used subsets of fiducial markers to solve for local alignments. An R-weighted back-projection program used the local alignments to compute a single reconstructed volume. Large area image data were thus accurately aligned despite nonhomogeneous geometrical changes that occurred in the specimen, because of electron beam damage over the course of the tilt series. The 3-D density distributions (tomograms) calculated from each set of aligned tilts were aligned with each other and combined to produce a single, high resolution (≈6 nm) 3-D reconstruction (12).

Dual axis 3-D reconstructions calculated in this manner from each of three serial 400-nm sections were aligned with one another as previously described (6), to produce a total reconstructed volume measuring $3.1 \times 4.7 \times 1.2\ \mu m^3$. Because one end of the digitized area frequently fell off the edge of the negative, reliable high resolution 3-D data in the reconstructed volume was effectively limited to the region analyzed in detail and modeled here ($3.1 \times 3.2 \times 1.2\ \mu m^3$).

3-D Modeling. Tomographic data were analyzed with IMOD software (13) by using Silicon Graphics computers (Silicon Graphics, Mountain View, CA). Organellar membranes, MTs, and vesicles were modeled and displayed in 3-D, essentially as described elsewhere (14, 6), with the following exceptions. Spherical vesicles (including dense core vesicles) were individually modeled by drawing a single contour around their circumference where the radius was maximal, as visualized in cross section. The area within this contour was used to determine the radius of an equivalent circle, and the contour was automatically replaced by a sphere of that radius. The size of each spherical vesicle was thus approximately represented in 3-D, allowing its surface area and volume to be calculated.

Clathrin coats on vesicles and budding profiles were readily identified by the presence of the clathrin lattice. Buds and vesicles with coats other than clathrin were not as readily distinguished from uncoated vesicles because of the facts that (*i*) there is a loss of resolution that accompanies increased section thickness when using the tomographic approach; (*ii*) COP coats are not so structurally distinct as clathrin (4); (*iii*) we omitted tannic acid (which enhances the visualization of COP coats) from the freeze-substitution regimen to resolve the membranes themselves more clearly; and (*iv*) reconstructing a large volume meant that the quality of preservation varied throughout the region under study, thus limiting local resolution in some small areas. We have therefore limited our classification of buds and vesicles to the broader categories of clathrin-positive and clathrin-negative.

Cellular structures modeled in 3-D were meshed and displayed as previously described (6). Because a 2.3-nm tomographic slice parallel to the plane of section corresponded to ≈3.8 nm of sample material before the section collapse that occurs on initial exposure to the electron beam (15), the *z*-dimension of our model was stretched by a factor of 1.66 to bring the total thickness of the model to 1.2 μm (i.e., three serial sections, each 400 nm thick). Membrane surface areas and volumes were then computed from the triangular meshes. As contours were placed in the middle of the membrane, the interior volume was computed by subtracting the surface area × 3.5 nm (half of the membrane's thickness) from the volumes inside the contours.

3-D Analysis. Spatial relationships among modeled objects were analyzed by measuring distances between objects in 3-D and computing an average density of neighboring items as a function of distance between objects (hereafter called spatial density analysis). Each item of a given kind was taken in turn as a reference object, and the distances to all nearby neighboring objects of a particular kind were measured (14). A neighbor density was obtained by dividing the number of items at a given range of distances by the approximate total volume at those distances from all such reference objects, where volume was estimated from the size of a shell at a given distance from an object.

Modeled objects were of three different kinds: spheres (e.g., vesicles), lines (e.g., MTs), and complex surfaces or compartments (e.g., tubulo-vesicular elements and cisternae). When a MT was a reference object, it was divided into regularly spaced (10-nm) subsegments, with closest approaches measured from each segment to assess multiple or extended close approaches between MTs and cisternal elements. Distances were measured from the central axis of MTs to the center of membranes or to the surfaces of spheres. "Complex surfaces" were defined by a mesh of triangles; each separate triangle was treated in turn as a reference or neighboring object.

In an ideal density analysis, nonrandom arrangements can be detected by a deviation from flatness in the calculated distributions. However, easily interpretable graphs were rarely obtained in the current analyses because of the constraints imposed by the many large structures in the volume studied and because distances were measured to extended rather than compact elements. It was thus critical to assess the graphs based on actual data, by comparing them with graphs based on randomly arranged items of equivalent shape and density.

Randomized data were prepared by shifting items through random displacements to new positions within the 3-D volume, rejecting only those displacements that shifted objects outside of the modeled region or resulted in collisions between objects. Up to 400 trials were necessary to find acceptable shifts. In some cases, not all items of a given type could be shifted. In such cases, density graphs computed from only the successfully shifted items ("shifted") were compared with graphs of those same items returned to their original positions ("deshifted").

Three sets of randomization controls were computed. First, both dense core and non-clathrin vesicles were moved to new positions in the modeled volume and not allowed to collide with any other existing element. From this arrangement, relations among these objects and between them and all others could be assessed. Second, endo-lysosomal compartments were shifted to random positions and not allowed to collide with MTs, Golgi cisternae, or the endoplasmic reticulum (ER). Nevertheless, ≈7%–14% of endo-lysosomal compartments could not be shifted to new positions after the rest had been. From the shifted items, relations among these elements and with MTs, cisternae, and the ER could be analyzed. Finally, MTs were shifted and constrained not to collide with Golgi cisternae or the ER.

On-Line Supplementary Material. Accompanying the figures presented here, QUICKTIME Movies 1–20, which are published as supplemental data on the PNAS web site, www.pnas.org, show either the 3-D tomographic slice data or 3-D model data incrementally rotated 360° around the *y* axis.

Results

3-D reconstructions were generated from fast frozen/freeze-substituted HIT-T15 cells to examine spatial relationships among the organelles involved in the synthesis, processing, and secretion of insulin under steady state conditions. Such reconstructions can readily be studied by viewing slices of the 3-D volume, each 3.8 nm thick and oriented parallel to the plane of the original microtome sections (Fig. 1*A*). These views resemble conventional electron micrographs, although they correspond to slices far thinner than can be cut with a microtome. Fig. 1*B* shows the boxed area in Fig. 1*A* at higher magnification, and reveals both the resolution of the reconstruction (the two leaflets of membrane bilayers can often be distinguished) and the quality of preservation achieved. Fig. 1*C* shows the same area with colored contours overlayed on some membranes to display a stage in the modeling process. Equivalent contours were drawn on every object of interest for each of the 315 slices in the tomogram to provide data for surface meshing and visualization, as described in *Materials and Methods* and presented in Fig. 2.

The Golgi. The Golgi in the modeled region comprises seven distinct cisternae that branch considerably through the reconstructed volume (Fig. 2) and encompass ≈70 μm^2 of membrane surface area. These cisternae will be referred to from cis to trans (i.e., from the outside to the inside of the curved Golgi ribbon as shown in Fig. 1*A*) as C1 through C7 (Fig. 2*A*). The orientation of the cis-trans axis was determined by the presence of numerous clathrin-coated profiles on C7 (Fig. 1 *B* and *C*). When this same Golgi is viewed in context with other modeled structures, one has an opportunity to visualize the dense packing of subcellular organelles, ribosomes, vesicles, and MTs in the cytoplasm of the Golgi region that is not afforded by fluorescence microscopy or conventional EM (Fig. 2*C*). Even though the Golgi region appears "crowded," ≈66% of this volume is calculated to represent cytoplasmic matrix, in that it lies outside the boundaries of the modeled structures.

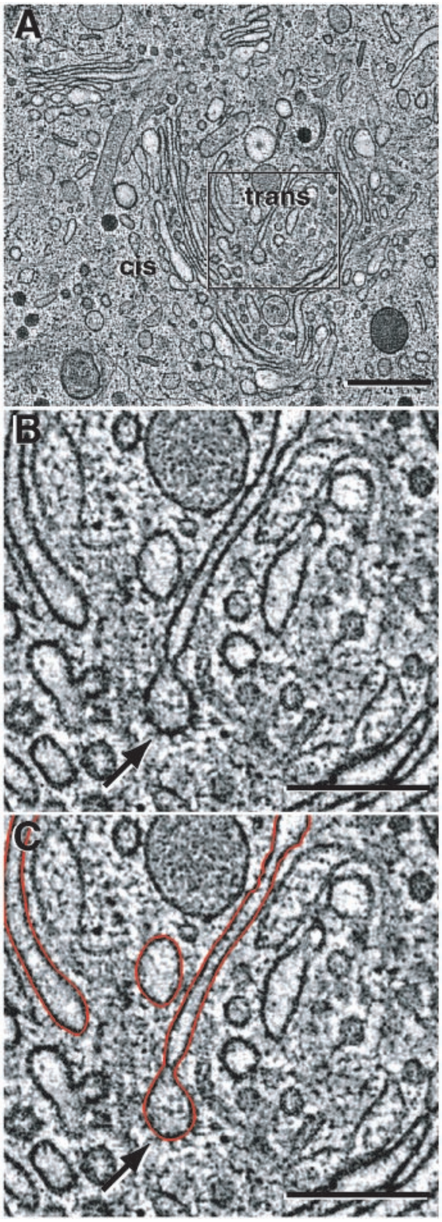

Fig. 1. 3-D reconstruction of part of the Golgi ribbon. (*A*) A 3.8-nm tomographic slice (slice 169) extracted from the 315 slices that together comprise the reconstructed volume. The area shown (3.1 × 3.2 μm^2) was modeled and analyzed in detail. Bar = 500 nm. The boxed area in *A* is shown at higher magnification in *B* and *C*. (*B* and *C*) Membranes were modeled by placing points along the bilayers, connecting the points with colored line segments, and building closed contours that delimited distinct membrane-bounded compartments and vesicles for each of the 315 tomographic slices. Arrow, clathrin-coated budding profile; cis and trans refer to the entry and exit faces of the Golgi ribbon. Bars = 250 nm.

The ER. The ER in the modeled region is a single, continuous organelle bounded by ≈45 μm^2 of membrane. Interestingly, the surface area:volume ratios of the ER and the Golgi are similar (76.6 and 71.8, respectively). Some regions of ER have numerous ribosomes bound whereas others are entirely devoid of ribosomes (Fig. 2*B*). The ER forms close contacts with each of C5, C6, and C7 (Fig. 2*B*). Remarkably, at several points, the ER traverses the entire Golgi stack via aligned openings in the cisternae and extends in opposite directions beyond the cis-most (C1) and trans-most (C7) Golgi cisternae (Fig. 2 *B* and *C*). The cisternal openings through which the ER is continuous across the Golgi stack correspond exactly with the openings through which tubules from C1 project through the stack into the trans Golgi region, although the Golgi and ER membrane tubules remain distinct. One region of the ER that flattens out and is closely apposed to C5 has numerous ribosomes bound on the membrane surface that is distal to the Golgi (Fig. 2*B*). This ER resembles the specialized trans ER characterized in fast frozen/freeze-substituted normal rat kidney and HepG2 cells (6, 16). It is noteworthy that the ER, which flattens against C5, is directly continuous with that which appears to be intimately associated with mitochondria situated near to the Golgi (Figs. 2*B* and 3*A*). In addition to the direct contact between the ER and trans Golgi cisternae and mitochondria, the ER forms numerous close

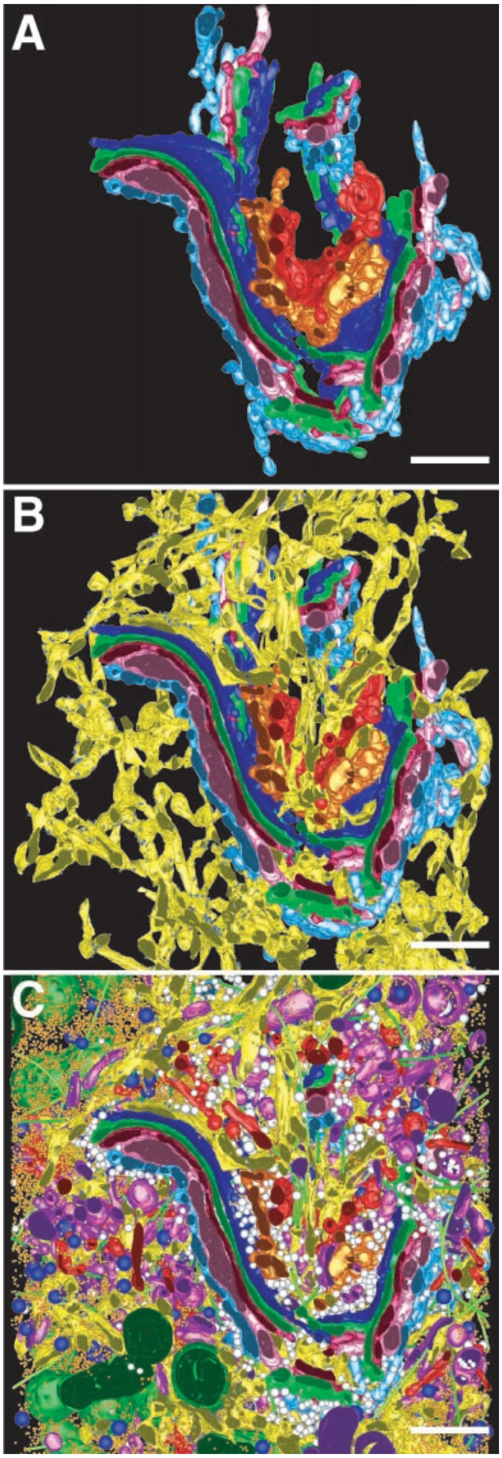

Fig. 2. 3-D model of the Golgi region. By using the software IMOD, each modeled object could be extracted and viewed in any given orientation and in context with any other object(s) to analyze complex morphologies with minimal ambiguity. (*A*) The seven cisternae that comprise the Golgi in the region modeled. C1, light blue; C2, pink; C3, cherry red; C4, green; C5, dark blue; C6, gold; C7, bright red. (*B*) The ER (yellow) traverses the Golgi stack at multiple points and extends in opposite directions beyond the cis-most and trans-most cisternae. (*C*) The Golgi displayed in the context of all organelles, vesicles, ribosomes, and MTs visible by EM in the modeled region. ER, yellow; membrane-bound ribosomes, blue; free ribosomes, orange; MTs, bright green; dense core vesicles, bright blue; clathrin-negative vesicles, white; clathrin-positive compartments and vesicles, bright red; clathrin-negative compartments and vesicles, purple; mitochondria, dark green. Bars = 500 nm.

physical associations with individual endo-lysosomal elements (Fig. 3*B*).

Vesicles. Numerous small (average diameter 52 nm), spherical vesicles ($n = 2{,}119$) were present in the Golgi region (Figs. 2*C* and 3*C*). These vesicles did not colocalize with endo-lysosomal compartments, clathrin-coated vesicles, or dense core vesicles (data not shown). Instead, most were situated close to Golgi cisternae and to a lesser extent the ER. We have not referred to these vesicles as "free" because most of them were unmistakably tethered to neighboring vesicles and/or Golgi membranes (Fig. 3*D*). In contrast, most of the 37 clathrin-positive and 97 clathrin-negative irregularly or oblong-shaped "vesicles" were clustered away from the Golgi (Fig. 3*E*). Of the 132 dense core vesicles (average diameter 100 nm; Fig. 3*F*), not one was attached to the Golgi.

Endo-lysosomal Compartments. Groups of tubulo-vesicular elements clustered in relatively close proximity to the Golgi were broadly classified as endo-lysosomal compartments (Figs. 3 *B* and *E* and 4*C*). These elements were subclassified first by the presence or absence of clathrin on their membranes. Clathrin-negative and clathrin-positive elements were subdivided further by morphology. Most clathrin-negative elements were relatively small, flattened saccules, ≈100–300 nm in diameter. A number of these projected tubules. In addition, numerous discrete tubules were present and many of these appeared flattened, consistent with the idea that they may once have been continuous with the flattened saccules.

Clathrin-positive elements most often took the form of tubulo-vesicular clusters that displayed clathrin coats on their numerous budding profiles. Clathrin-coated free vesicles ($n = 37$; ≤ 100 nm in diameter) and tubules were frequently found clustered together with these larger, highly branched structures (Fig. 3*D*). Most of the relatively nondescript clathrin-negative compartments were oblong and ranged in size from 100–500 nm. A number of these contained multiple vesicles within their compartmental lumen.

MT-Organellar Relationships. MTs ($n = 80$) with a total combined length of over 80 μm were modeled to characterize and quantify *in situ* associations between the MT cytoskeleton and different organelles. The paths of some of these MTs closely followed (separated by ≤ 30 nm) the membranes of C1 (Fig. 4*A*), the ER (Fig. 4*B*), and endo-lysosomal compartments (Figs. 4*C* and 5*D*). The extent of close approach (number of approaches ≤ 30 nm) between MTs and C1 (Figs. 4*A* and 5*A*) was ≈8- to 15-fold greater than between MTs and C2–C7 (data not shown). MTs traversed Golgi stacks via non-compact regions and cisternal openings. Likewise, the extent of close approach between MTs and the ER was significant (1522 of the 10-nm MT subsegments were within 30 nm of ER membranes; Figs. 4*B* and 5*C*). However, the nature of these physical arrangements differed considerably from that observed between MTs and C1, or MTs and endo-lysosomal compartments. The paths of individual MTs appeared to follow the membranes of C1 and some endo-lysosomal compartments over considerable distances. In one case, the path of a membrane tubule ≈1 μm long paralleled the path of a MT over a distance of ≈250 nm, separated from it over this distance by less than 30 nm (Fig. 4*C*). In contrast, the ER frequently looked as although it was anchored along MTs. ER membranes were bridged to MTs at a few points, but for the most part they were not in direct association (Fig. 4*B*). It often appeared as if ER membranes were stretched from one MT to another, secured only by the small points of direct contact. Spatial density analysis of dense core vesicles and MTs (Fig. 4*D*) did not provide evidence of significant associations between these objects within the modeled region.

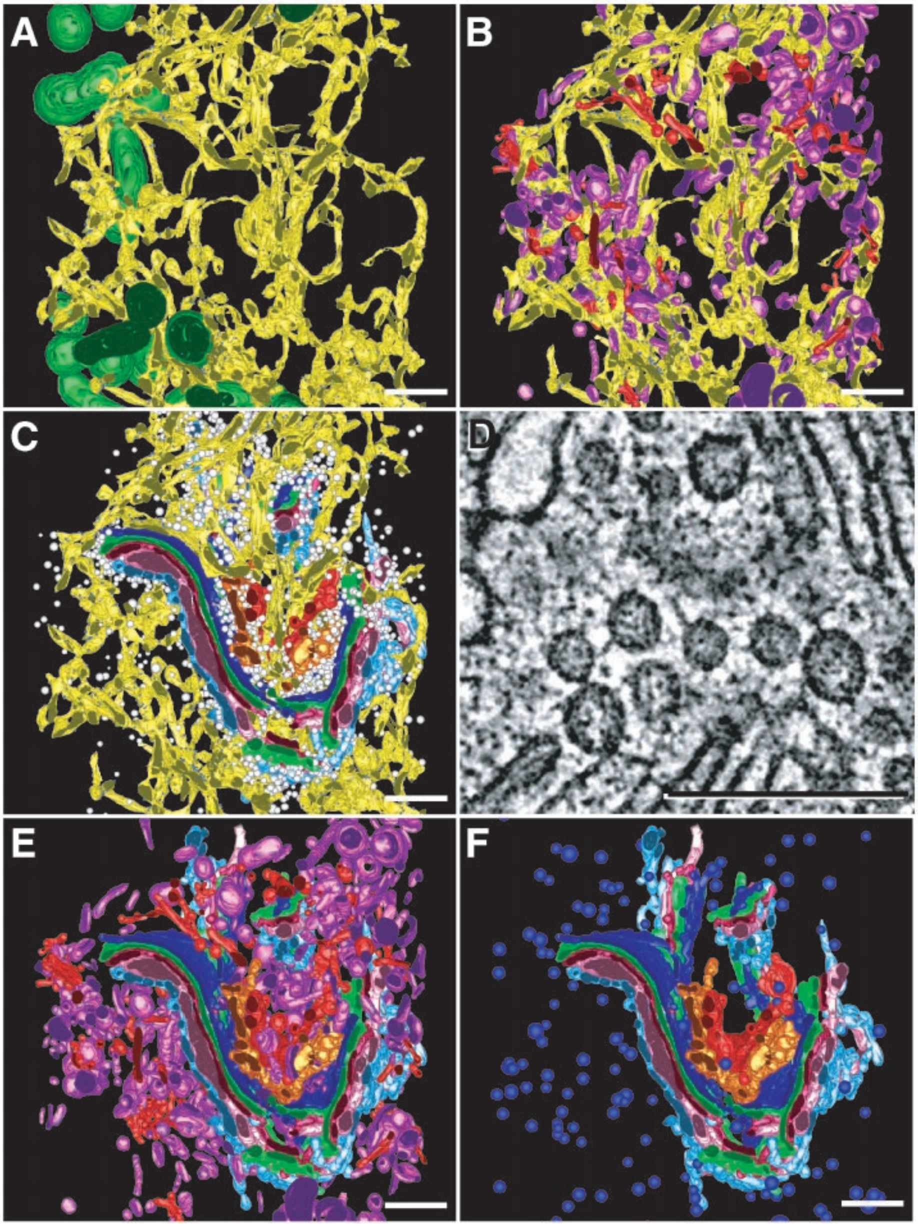

Fig. 3. Structural evidence for physical relationships among different organelles in the modeled region. The ER is closely apposed to mitochondria (dark green) (*A*), clathrin-positive (red) and clathrin-negative (purple) endo-lysosomal compartments (*B*). (*C*) Here, 2,119 small (average diameter 52 nm), spherical, non-clathrin vesicles (white) were distributed close to the Golgi and ER. (*D*) Higher magnification image extracted from tomographic data showing the numerous tethers connecting small vesicles to each other and to Golgi membranes. Bar = 250 nm. (*E*) Subsets of endo-lysosomal compartments with distinct morphological profiles were clustered together in the Golgi region. (*F*) Here, 132 dense core vesicles (bright blue; average diameter 100 nm) were present in the Golgi region but were apart from the Golgi stack. Bars = 500 nm.

The orientations of MTs with respect to the centriole pair (located just outside of the reconstructed region) was somewhat haphazard. Computational analysis of MT path segments projected up to 1 μm outside of the modeled region revealed that MTs in this region of the cell did not appear to project to/from the centrosome (data not shown). Further, the daughter centriole of the pair, the one visible in the reconstructed region (data not shown), showed only a single MT associated with it.

Discussion

The fundamental mechanisms of how molecules move to, through, and from the Golgi, and how structural changes in this and surrounding organelles relate to these events remain poorly understood and somewhat controversial (17–21). There are four major reasons for this. First, although *in vivo* imaging by using the green fluorescent protein (GFP) tag has helped to elucidate the dynamics and kinetics of membrane transport in live cells (22), light microscopy does not provide the resolution necessary to distinguish all of the elements of the Golgi ribbon, the cisternal origins of associated tubules, or the presence of vesicles. For example, although small vesicles like those we show clustered near Golgi cisternae (Fig. 3*C*) could be detected if they were alone, they are distributed in the model with a density of $\approx$1 sphere/150 nm in all three dimensions. A fluorescent label on such vesicles would appear in the light microscope simply as a background glow. Further, the resolution attained by light

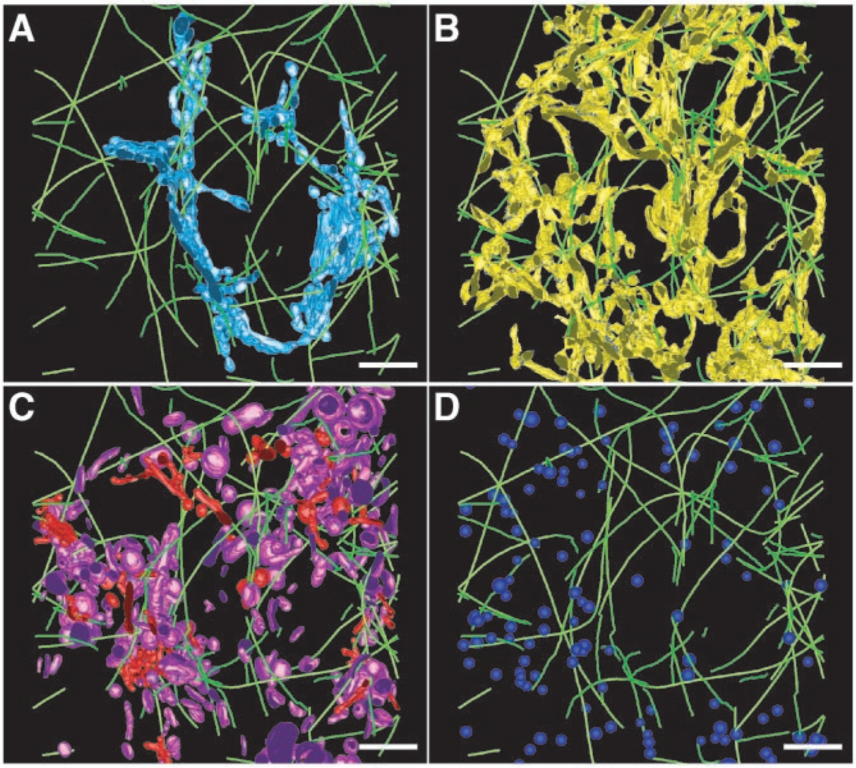

Fig. 4. The MT cytoskeleton associates with membranes of the Golgi, ER, and endo-lysosomal compartments. The paths of MTs (bright green) closely followed and occasionally formed contacts with the membranes of C1 (light blue; *A*) and the ER (yellow; *B*). Clathrin-positive (red) and clathrin-negative (purple) compartments (*C*) and dense core vesicles (bright blue; *D*) in the reconstructed volume were modeled so that *in situ* spatial relationships between these elements and MTs could be reliably quantified and assessed. Bars = 500 nm.

microscopy can be related to the brightness of the fluorescent signal. When the fluorescence is intense, the signal can appear significantly larger than the actual structure, and, when the signal is low, the structure may not be seen.

Second, most biological EM data come from two-dimensional images of thin-sectioned material, from which 3-D structural characteristics can be only approximated. Even when 3-D reconstructions are generated from serial thin sections, the structure of the Golgi is often so convoluted that fine details of connectivity are lost or not reliably observed from one section to the next. Third, most studies of the Golgi have used classical chemical fixation methods that are largely inadequate for preserving this organelle's highly dynamic and labile structure. Finally, much of the current dogma regarding Golgi structure/function relationships is based on immunolabeling studies at both the light and EM levels; these techniques suffer from most, if not all, of the limitations discussed above.

Ultrastructural tools that improve the preservation and imaging of organellar relationships are now available. Fast freezing followed by freeze-substitution preserves cellular constituents in a state that reliably reflects the *in vivo* situation (23–25). Furthermore, these techniques provide a means with which to capture and visualize highly dynamic processes at the ultrastructural level by virtue of the fact that all cellular events are arrested within 10–20 ms (8). We have combined these methods with EM tomography to structurally dissect part of a regulated secretory cell in the steady state at a level of clarity and reliability not afforded by other methods. Thus, by modeling the Golgi and neighboring organelles, vesicles and MTs in 3-D at $\approx$6 nm resolution, we provide new structural data with which to address existing models for membrane traffic and regulated secretion in mammalian cells.

The Dynamic Golgi. The notion of the Golgi as a dynamic rather than static organelle has regained favor with the membrane-trafficking community over the past decade. Revised models for membrane trafficking into and out of the Golgi attempt to relate the wealth of biochemical data, generated via the molecular dissection of membrane trafficking pathways (26–28), to more recent structural data. These models propose that the mechanisms of cisternal progression-maturation, trafficking via membrane tubules, and vesicle-mediated transport all play a role in Golgi membrane trafficking (17–19, 21, 29). In addition to the numerous (>2,000) small vesicles distributed close to Golgi membranes in the present study, several tubules from C1 projected through the stack, via aligned holes in Golgi cisternae C2–C5, into the trans Golgi region. Whether these tubules function in moving cargo forwards through the Golgi stack, or mediate the retrograde transport of early Golgi/ER processing enzymes back to the cis Golgi/ER interface remains unclear. Tubules that extended away from C1 in the cis direction and which presumably operate in transport between the Golgi and ER (30) were also present. However, no membrane tubules connecting cisternae at different levels of the Golgi stack were present. Further, all of the membrane tubules observed were consistent with the "blind-ended tubules" described by Weidman *et al.* (3), in that they projected away from the edge of the cisterna, but did not form fenestrations at the edges of cisternae by looping back and fusing with the periphery of the cisterna.

Dense Core Vesicles. Secretory granules, visible by EM as dense core vesicles, represent a major post-Golgi compartment in regulated secretory cells. In the present study, 132 such vesicles were observed. The collective membrane area of these granules (4.0 μm^2) is equivalent to that of C6 (4.1 μm^2) and is larger than

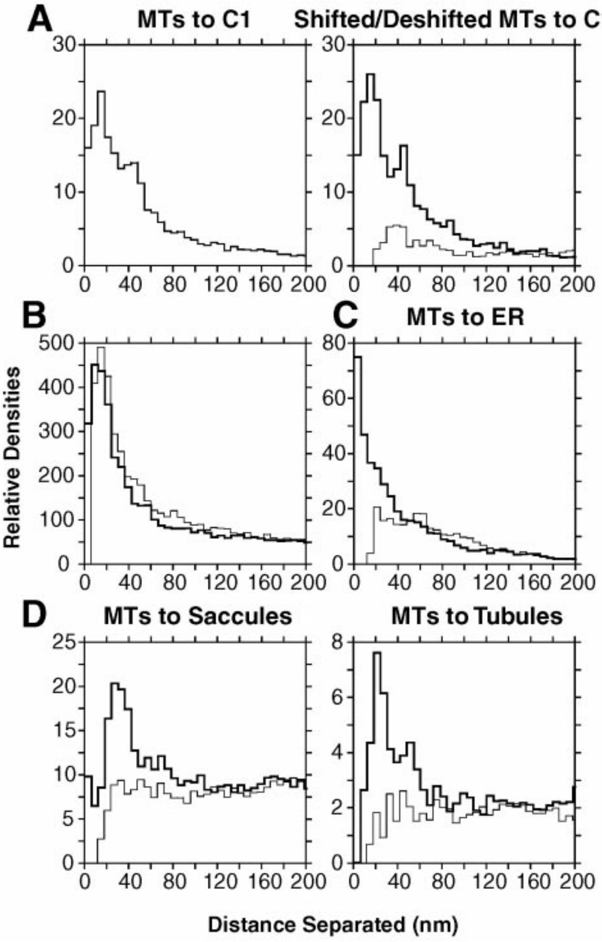

Fig. 5. Analysis of distances between modeled objects in the reconstructed volume. To determine the significance of peaks in density analysis graphs, the real distributions of objects were compared with randomized distributions of the same objects. Peaks in the real spatial distributions (bold lines) that are substantially above the randomized distributions (thin lines) are likely to represent specific associations. (*A Left)* Histogram showing the real distribution of distances from 10-nm subsegments of MTs to C1. (*Right*) Because only 72% of the MTs could be shifted randomly in 3-D without colliding with other objects, the density distribution of only those MTs that could be shifted and thereby randomized for the analysis (''shifted'') is compared with their distribution after being returned to their original positions (''deshifted''). (*B*) The density of clathrin-negative endo-lysosomal compartments around non-clathrin vesicles provides an example of a null relationship. The peak in the real distribution is indistinguishable from that observed in randomized distributions of non-clathrin vesicles, suggesting that there is no specific relationship between them. Spatial density analysis revealed strong evidence for specific associations between MTs and the ER (*C*), and between MTs and some morphological subsets of elements broadly classified as endo-lysosomal compartments (*D*), respectively.

that of C7 (3.7 μm^2). Remarkably, not a single granule was attached to the Golgi in this reconstruction. However, in the absence of a metabolic demand for insulin, the Golgi is quiescent with respect to processing, packaging, and secreting insulin (31). This result was supported by our finding that dense core vesicles did not appear to associate with MTs to any significant extent (data not shown). The fact that the Golgi appears to have been actively budding vesicular and/or tubular profiles at every level of the stack the instant the cell was frozen, combined with the presence of over 2,000 small vesicles in close proximity to Golgi membranes, suggests that, although no secretory granules appear to have been forming when the cell was frozen, the Golgi modeled here was far from dormant with respect to other membrane traffic.

Endo-Lysosomal Compartments. We broadly classified the large number of compartments clustered in relatively close proximity to the Golgi as endo-lysosomal compartments. One major subset consists of highly branched tubular elements that display numerous clathrin-coated profiles. These elements resemble the cactus-like endosomal structures described by Stoorvogel *et al.* (32). Further, endosomal clathrin-coated tubules and buds could be distinguished from the clathrin-coated budding profiles and tubules of C7 by virtue of their size ($\leq$80 nm vs. 100 nm in diameter; 32). This finding, along with the distinctive morphologies of multivesicular compartments, allowed us to confidently identify a number of these as elements of the endo-lysosomal pathway. The highly furcated nature of these elements, together with the presence of discontinuous vesicles and tubules of similar diameters ($\leq$80 nm in diameter) clustered close by, suggests that these elements are highly dynamic. Spatial density analysis provided no evidence of significant association between clathrin-positive elements and MTs (data not shown). Small, tubulo-saccular objects constituted the bulk ($>$200) of these compartments. These saccules were clustered with discrete tubules of varying lengths and widths, along with other endo-lysosomal compartments. The tubules may have originated either directly from the trans Golgi or from these tubulo-saccular objects. Spatial density analysis revealed that these saccules and tubules associated significantly with MTs (Figs. 4*C* and 5*D*). In addition to clustering with each other, these elements were concentrated in clusters very close to the Golgi ribbon (Fig. 3*E*).

ER-Organellar Relationships Mediated By Close Contacts. Two morphologically distinct regions of the ER closely appose each of the three trans Golgi elements C5, C6, and C7. The first type of ER has a cisternal appearance, with ribosomes bound on only one surface; it flattens out to closely follow the cisternal membrane of C5. This first type resembles ER membranes that have been described by others in close association with the trans Golgi (6, 33–36). The second kind of ER traverses the Golgi stack and is almost entirely devoid of bound ribosomes; its convoluted membranes form close contacts with C5, C6, and C7 in the heart of the trans Golgi region. This ER corresponds to descriptions of smooth ER postulated to function in lipid metabolism at the trans Golgi face (37). Such sites of close apposition between the ER and trans Golgi have been proposed to facilitate molecular exchange between these two organelles (36, 6), and may account for the trans-first scattering of Golgi enzymes after MT depolymerization (38).

The ER that adheres to C5 is continuous with that which forms close contacts with mitochondria. Interestingly, close contacts between smooth subdomains of the ER and mitochondria have been shown to be required both for maintaining mitochondrial structure and for mediating lipid transfer between the two organelles (39, 40). Thus, the close contacts we observe between membranes of the ER and trans Golgi, mitochondria, and endo-lysosomal compartments may represent part of a yet uncharacterized, non-vesicle-mediated transfer mechanism between these organelles.

A role for specialized ER membranes in lipid synthesis/exchange at the trans Golgi may also help to address the question of why trans Golgi elements dissociate from earlier cisternae (34). If lipid exchange at the ER/trans Golgi interface plays a role in the segregation of different cargoes for distinct destinations, then the movement of trans elements out of register with the stack may be prerequisite for this and for subsequent fragmentation. Lipid rafts have been proposed to function in sorting proteins and lipids from the trans Golgi to the apical plasma membrane in both polarized and nonpolarized cells (41, 42). An engaging hypothesis is that close contacts between the ER and trans Golgi contribute to the formation of lipid rafts in the trans Golgi. Collectively, these findings lead us to propose that the ER plays an important role in membrane traffic from the Golgi.

The MT Cytoskeleton. A unique aspect of this study is our ability to model individual MTs and analyze their *in situ* relationships with organelles and vesicles in the Golgi region in 3-D (Figs. 4 and 5). MTs play an important role in membrane trafficking to and from the Golgi (43, 44). However, the precise mechanisms by which MTs maintain the organization of the Golgi and ER remain unclear. Although we found no evidence to support the notion that MTs provide a structural framework for the Golgi *per se*, we did find that MTs associated specifically with C1. This finding supports the idea that MTs function in membrane trafficking at the cis aspect of the Golgi (45). Intriguingly, we also found that MTs traversed the Golgi stack via cisternal openings at multiple points. Whereas MTs do not appear to be required for the *de novo* formation of the ER network *in vitro* (46), the nature of the associations between the ER and MTs observed here supports a role for MTs in the positioning and maintenance of the ER network *in vivo* (47). The organization of MTs in our model is at odds with the commonly held view that cytoplasmic MTs in mammalian cells radiate from the interphase centrosome. The orientation of MTs in our data is, however, more representative of interphase epithelial cells than the images presented in the literature as conventional wisdom. Cytoplasmic MTs grow from the centrosome in post-mitotic cells, but during interphase this radial array is generally lost, particularly in epithelia (48). Many MTs in such cultured cells have their minus ends associated with the nuclear envelope, not the pericentriolar material.

Concluding Remarks. By providing a 3-D snapshot of vesicles, organellar and compartmental membranes, and the MT cytoskeleton in a fast frozen HIT-T15 cell, and revealing the physical associations between these structures captured at the instant the cell was frozen, these data provide exciting insights into the complexity of organellar relationships in the Golgi region of a regulated secretory cell. The combination of these high resolution techniques with methods to localize specific molecules *in situ* in 3-D should allow us to define precisely the temporal and spatial coordinates of regulated secretion and exocytosis in future studies, and to test new hypotheses related to these events in mammalian cells.

We thank Tom Giddings, Mark Ladinsky, Mary Morphew, and Eileen O'Toole for technical advice and assistance, Andrew Staehelin for use of the High Pressure Freezer, and John Hutton and Tina Wasmeier for useful discussions. We also thank the staff and directors of the Wadsworth Center's Resource for the Visualization of Biological Complexity for the use of their facilities, and for help in collecting some of these data. The Boulder Laboratory for 3-D Fine Structure and the Resource for the Visualization of Biological Complexity are supported by National Institutes of Health National Center for Research Resources/Biomedical Technology Grants RR 00592 and RR 01229, respectively. This work was also supported by National Institutes of Health Grant GM42629 to K.E.H. and Program Project Grant P01GM61306 to J.R.M. B.J.M. is a Juvenile Diabetes Research Foundation International (JDRF) Postdoctoral Fellow.

1. Lindsey, J. D. & Ellisman, M. H. (1985) *J. Neurosci.* **5,** 3124–3134.
2. Tanaka, K. & Fukudome, H. (1991) *J. Electron Microsc. Technol.* **17,** 15–23.
3. Weidman, P., Roth, R. & Heuser, J. (1993) *Cell* **75,** 123–133.
4. Ladinsky, M. S., Kremer, J. R., Furcinitti, P. S., McIntosh, J. R. & Howell, K. E. (1994) *J. Cell Biol.* **127,** 29–38.
5. Rambourg, A. & Clermont, Y. (1997) in *The Golgi Apparatus*, eds. Berger, E. G. & Roth, J. (Birkhauser, Basel), pp.37–61.
6. Ladinsky, M. S., Mastronarde, D. N., McIntosh, J. R., Howell, K. E. & Staehelin, L. A. (1999) *J. Cell Biol.* **144,** 1135–1149.
7. Heuser, J. E., Reese, T. S. & Landis, D. M. (1976) *Cold Spring Harbor Symp. Quant. Biol.* **40,** 17–24.
8. Gilkey, J. C. & Staehelin, L. A. (1986) *J. Electron Microsc. Technol.* **3,** 177–210.
9. Santerre, R. F., Cook, R. A., Crisel, R. M., Sharp, J. D., Schmidt, R. J., Williams, D. C. & Wilson, C. P. (1981) *Proc. Natl. Acad. Sci. USA* **78,** 4339–4343.
10. Breant, B., Lavergne, C., Astesano, A., Ferrand, N., Asfari, M., Boissard, C., Anteunis, A. & Rosselin, G. (1992) *Mt. Sinai J. Med.* **59,** 175–185.
11. Yorde, D. E. & Kalkhoff, R. K. (1986) *J. Histochem. Cytochem.* **34,** 1195–1200.
12. Mastronarde, D. N. (1997) *J. Struct. Biol.* **120,** 343–352.
13. Kremer, J. R., Mastronarde, D. N. & McIntosh, J. R. (1996) *J. Struct. Biol.* **116,** 71–76.
14. McDonald, K. L., O'Toole, E. T., Mastronarde, D. N. & McIntosh, J. R. (1992) *J. Cell Biol.* **118,** 369–383.
15. Luther, P. K., Lawrence, M. C. & Crowther, R. A. (1988) *Ultramicroscopy* **24,** 7–18.
16. Hess, M. W., Muller, M., Debbage, P. L., Vetterlein, M. & Pavelka, M. (2000) *J. Struct. Biol.* **130,** 63–72.
17. Mellman, I. & Simons, K. (1992) *Cell* **68,** 829–840.
18. Mironov, A. A., Weidman, P. & Luini, A. (1997) *J. Cell Biol.* **138,** 481–484.
19. Bannykh, S. I., Nishimura, N. & Balch, W. E. (1998) *Trends Cell Biol.* **8,** 21–25.
20. Farquhar, M. G. & Palade, G. E. (1998) *Trends. Cell Biol.* **8,** 2–10.
21. Glick, B. S. & Malhotra, V. (1998) *Cell* **95,** 883–889.
22. Hirschberg, K., Miller, C. M., Ellenberg, J., Presley, J. F., Siggia, E. D., Phair, R. D. & Lippincott-Schwartz, J. (1998) *J. Cell Biol.* **143,** 1485–1503.
23. Linder, J. C. & Staehelin, L. A. (1979) *J. Cell Biol.* **83,** 371–382.
24. Hirokawa, N. & Kirino, T. (1980) *J. Neurocytol.* **9,** 243–254.
25. Ornberg, R. L. & Reese, T. S. (1980) *Fed. Proc.* **39,** 2802–2808.
26. Rothman, J. E. (1981) *Science* **213,** 1212–1219.
27. Balch, W. E., Dunphy, W. G., Braell, W. A. & Rothman, J. E. (1984) *Cell* **39,** 405–416.
28. Malhotra, V., Serafini, T., Orci, L., Shepherd, J. C. & Rothman, J. E. (1989) *Cell* **58,** 329–336.
29. Pelham, H. R. & Rothman, J. E. (2000) *Cell* **102,** 713–719.
30. de Figueiredo, P., Drecktrah, D., Katzenellenbogen, J. A., Strang, M. & Brown, W. J. (1998) *Proc. Natl. Acad. Sci. USA* **95,** 8642–8647.
31. Schnell Landstrom, A. H., Andersson, A. & Borg, L. A. (1991) *Metabolism* **40,** 399–405.
32. Stoorvogel, W., Oorschot, V. & Geuze, H. J. (1996) *J. Cell Biol.* **132,** 21–33.
33. Hand, A. R. & Oliver, C. (1977) *Histochem. J.* **9,** 375–392.
34. Pavelka, M. & Ellinger, A. (1983) *Eur. J. Cell Biol.* **29,** 253–261.
35. Craig, S. & Staehelin, L. A. (1988) *Eur. J. Cell Biol.* **46,** 81–93.
36. Thorne-Tjomsland, G., Clermont, Y. & Tang, X. M. (1991) *Biol. Cell* **71,** 33–41.
37. Novikoff, A. B. (1976) *Proc. Natl. Acad. Sci. USA* **73,** 2781–2787.
38. Yang, W. & Storrie, B. (1998) *Mol. Biol. Cell* **9,** 191–207.
39. Vance, J. E. (1990) *J. Biol. Chem.* **265,** 7248–7256.
40. Prinz, W. A., Grzyb, L., Veenhuis, M., Kahana, J. A., Silver, P. A. & Rapoport, T. A. (2000) *J. Cell Biol.* **150,** 461–474.
41. Mellman, I., Yamamoto, E., Whitney, J. A., Kim, M., Hunziker, W. & Matter, K. (1993) *J. Cell Sci. Suppl.* **17,** 1–7.
42. Keller, P. & Simons, K. (1997) *J. Cell Sci.* **110,** 3001–3009.
43. Kreis, T. E. (1990) *Cell. Motil. Cytoskeleton* **15,** 67–70.
44. Cole, N. B. & Lippincott-Schwartz, J. (1995) *Curr. Opin. Cell Biol.* **7,** 55–64.
45. Presley, J. F., Cole, N. B., Schroer, T. A., Hirschberg, K., Zaal, K. J. & Lippincott-Schwartz, J. (1997) *Nature (London)* **389,** 81–85.
46. Dreier, L. & Rapoport, T. A. (2000) *J. Cell Biol.* **148,** 883–898.
47. Lee, C. & Chen, L. B. (1988) *Cell* **54,** 37–46.
48. Keating, T. J. & Borisy, G. G. (1999) *Biol. Cell* **91,** 321–329.